RESEARCH ARTICLE

3D Printing of Arbitrary Perovskite Nanowire Heterostructures

Mojun Chen, Zhiwen Zhou, Shiqi Hu, Nan Huang, Heekwon Lee, Yu Liu, Jihyuk Yang, Xiao Huan, Zhaoyi Xu, Sixi Cao, Xiang Cheng, Ting Wang, Siu Fung Yu, Barbara Pui Chan, Jinyao Tang, Shien-Ping Feng,* and Ji Tae Kim*

Deterministic integration of arbitrary semiconductor heterostructures opens a new class of modern electronics and optoelectronics. However, the realization of such heterostructures continues to suffer from impracticality, requiring energy- and labor-intensive, time-consuming fabrication processes. Here a 3D printing approach to fabricate freestanding metal halide perovskite nanowire heterostructures with a high degree of control over shape and composition is demonstrated. These features arise from freeform guiding of evaporation-driven perovskite crystallization by a femtoliter precursor meniscus formed on a printing nozzle. By using a double-barreled nanopipette as a printing nozzle, "all-at-once" heterostructure fabrication is achieved within seconds. The 3D-printed perovskite nanowire heterojunctions with multiple emission colors provide exciting optical functionalities such as programmable color mixing and encryption at the single nanopixel level. This "lithography-free" additive approach opens up the possibility to freely design and realize heterostructure-based devices without the constraints of traditional manufacturing processes.

1. Introduction

Metal halide perovskites have emerged as promising tunable semiconductor materials due to their excellent properties such as large optical absorption,[1–3] high carrier mobility,[4–6] long carrier diffusion length,[7–9] and low-temperature solution pro-

cessability.[10–13] Significant research efforts have been made to realize perovskite-based solid-state devices for photovoltaic and light-emitting applications.[14–21] A fundamental task for practical optoelectronic applications is to form a heterostructure with control over size, shape, and halide composition.[22–29] However, traditional semiconductor manufacturing processes are not suitable for perovskites.[30–35]

Unconventional sequential approaches have been devised to create perovskite heterostructures. Interdiffusion-controlled sequential growth[36] and growth-and-transfer[27] methods offer solution-phase routes to fabricate perovskite heterostructures. For the sequential gas-phase growth of heterostructures, laser-induced spinodal decomposition[37] and magnetic-pulling[38] have been employed. Selected-area anion exchange at particular positions in perovskite nanowires can produce heterostructures with a fine-tuning of the chemical compositions and electronic properties.[22,39] The localized anion-exchange area is made by a multiple sequential process including transfer, spin coating, and electron-beam (E-beam) lithography.[22] However, these approaches continue to suffer from the technological challenges associated

M. Chen, Z. Zhou, S. Hu, N. Huang, H. Lee, Y. Liu, J. Yang, X. Huan, Z. Xu, S. Cao, B. P. Chan, J. T. Kim
Department of Mechanical Engineering
The University of Hong Kong
Hong Kong 999077, China
E-mail: jtkim@hku.hk
M. Chen
Smart Manufacturing Thrust
Systems Hub
The Hong Kong University of Science and Technology
Guangzhou 511458, China

M. Chen
Department of Mechanical and Aerospace Engineering
The Hong Kong University of Science and Technology
Hong Kong 999077, China
Z. Zhou
Department of Electronic Engineering
Chinese University of Hong Kong
Hong Kong 999077, China
X. Cheng, J. Tang
Department of Chemistry
The University of Hong Kong
Hong Kong 999077, China
T. Wang, S. F. Yu
Department of Applied Physics
The Hong Kong Polytechnic University
Hong Kong 999077, China
S.-P. Feng
Department of Advanced Design and Systems Engineering
City University of Hong Kong
Hong Kong 999077, China
E-mail: tony.feng@cityu.edu.hk

**ADVANCED
SCIENCE NEWS**

www.advancedsciencenews.com

**ADVANCED
FUNCTIONAL
MATERIALS**

www.afm-journal.de

with limited shaping capability, process complexity, and time-inefficiency (process over tens of hours).

In this work, we harness 3D printing for fabricating perovskite nanowire heterostructures with programmed shape and material composition. Taking an additive manufacturing approach offers not only a high degree of control over shape and composition but also an unprecedented process simplicity.[40–42] Our 3D printing method is devised to exploit a femtoliter precursor ink meniscus to guide evaporation-driven crystallization in three-dimensions, forming a freestanding, arbitrary $CH_3NH_3PbX_3$ (X = Cl,Br,I) perovskite nanostructure. Furthermore, the use of a double-barreled nanopipette as a dual-nozzle enables "all-at-once" fabrication of a heterostructure with designed halide composition within seconds. We demonstrate the capability of the 3D-printed nanowire heterojunctions for color mixing and multicolor encryption at the single-pixel level without sacrifice of spatial resolution. Although in this work we restrict ourselves to metal halide perovskites, the method can be generalized for a wide range of solution-processable materials, creating semiconductor nanowire heterojunctions for highly integrated electronic and photonic devices.

2. Results and Discussion

Figure 1a depicts our 3D printing process for fabricating a free-standing perovskite nanowire heterojunction. To print two different perovskite compositions in a single-process platform, a double-barreled nanopipette is used as a dual printing nozzle. The double-barreled pipette is fabricated by a programmed heat-pulling process, followed by focused ion beam (FIB) cutting to create a height difference between two barrel tips. This stepped geometry is designed so that one of the tips starts printing first, allowing a sequential dual printing. The double-barreled pipette filled with two different precursor inks, for example, $CH_3NH_3Br + PbBr_2$ ink dissolved in 1:1 (volume ratio) dimethyl sulfoxide (DMSO):N,N-dimethylformamide (DMF) solvent for the longer barrel and $CH_3NH_3I + PbI_2$ ink for the shorter one, is prepared. When the longer barrel tip touches a silicon (Si) substrate first, a femtoliter ink meniscus containing $CH_3NH_3Br + PbBr_2$ is formed at the region of contact. Rapid evaporation of the solvent promotes the crystallization of $CH_3NH_3PbBr_3$ inside the meniscus, and its spatial guiding by
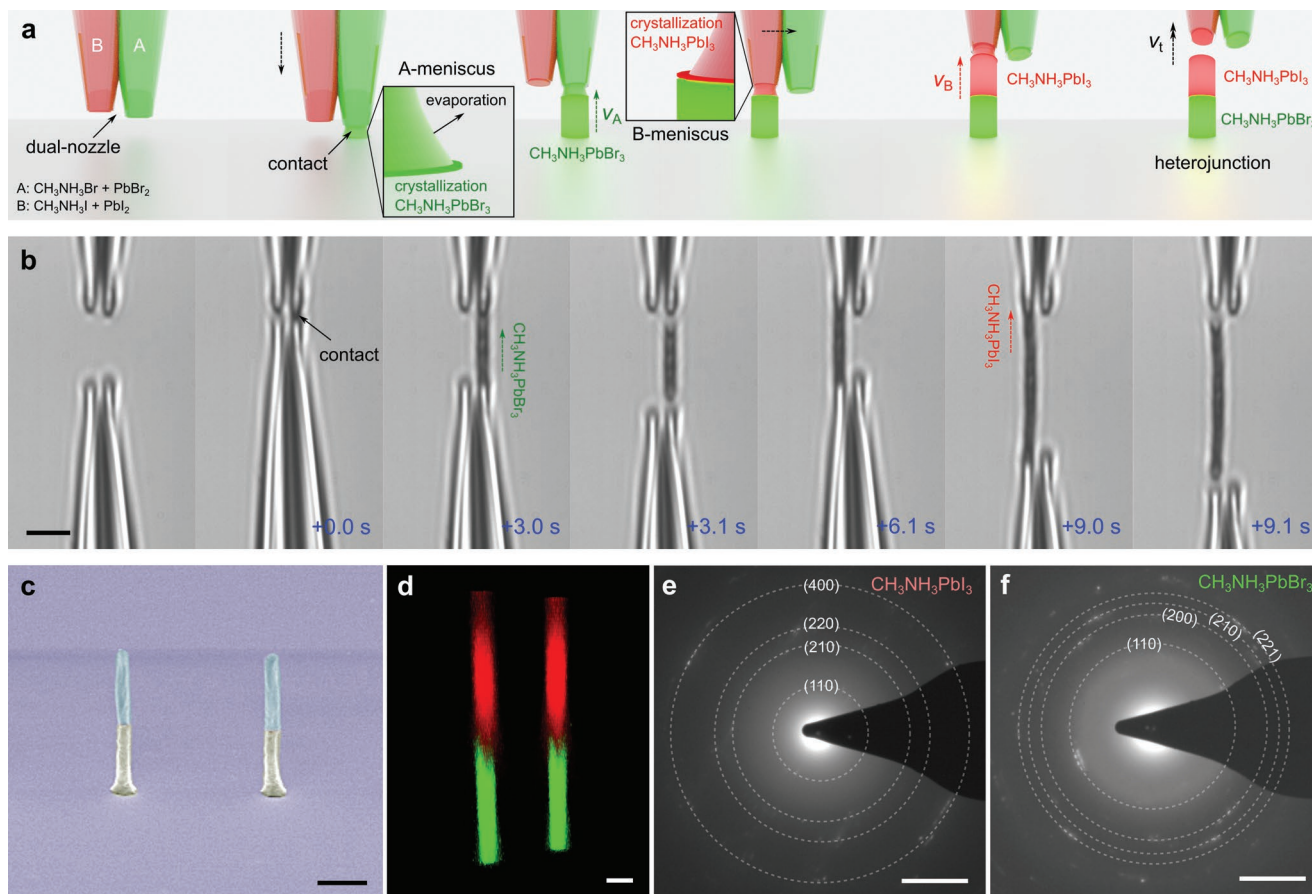

Figure 1. 3D printing of perovskite nanowire heterojunctions. a) Scheme illustrating a series of sequential steps of meniscus-guided 3D printing of a freestanding perovskite heterojunction nanowire. A double-barreled nanopipette filled with two different precursor inks (for example, ink A: $CH_3NH_3Br + PbBr_2$, ink B: $CH_3NH_3I + PbI_2$) is used. The geometry of the pipette is designed to allow one of two barrel tips to start printing. The printing process of each heterojunction segments consists of i) the formation of a femtoliter ink meniscus, ii) the continuous guiding of perovskite crystallization by moving the meniscus under solvent evaporation, and iii) the termination of the crystal growth. b) Corresponding optical micrographs of the 3D printing process. Entire printing process is completed in ten seconds (scale bar: 5 μm). c–f) 3D printed, freestanding $CH_3NH_3PbBr_3$–$CH_3NH_3PbI_3$ heterojunctions. c) Corresponding false-colored FE-SEM image (scale bar: 2 μm). d) 3D confocal PL image (scale bar: 2 μm). e) SAED pattern of the $CH_3NH_3PbI_3$ segment (scale bar: 2 1/nm). f) SAED pattern of the $CH_3NH_3PbBr_3$ segment (scale bar: 2 1/nm).

moving the pipette with a speed of $\approx\mu m\ s^{-1}$ leads to continuous and localized crystal growth. A freestanding $CH_3NH_3PbBr_3$ nanowire with a tailored length, which is one side of a heterojunction, is produced after terminating the growth by an abrupt increase in the pipette moving speed. To continue printing the other side, the barrel tip filled with $CH_3NH_3I + PbI_2$ ink physically contacts the top of the grown nanowire, forming a new meniscus. By subsequent meniscus guiding of $CH_3NH_3PbI_3$ growth, a freestanding $CH_3NH_3PbBr_3$–$CH_3NH_3PbI_3$ heterojunction nanowire is fabricated. As shown in a series of optical micrographs in Figure 1b, the entire printing only took 9.1 s, without the need for additional intricate processes such as transfer, spin coating, and lithography that require hours.

Figure 1c–f shows the characteristics of the printed $CH_3NH_3PbBr_3$–$CH_3NH_3PbI_3$ nanowire heterostructure. The well-defined diameter and height are 600 nm and 2 μm, respectively, as shown in the field-emission scanning electron microscope (FE-SEM) image of Figure 1c. Its two-color emission feature with a sharp, clear interface was confirmed by confocal photoluminescence (PL) imaging under the laser excitation of $\lambda = 364$ nm (Figure 1d). The emission peak centers for each segments were 535 nm (Figure S1a, Supporting Information) and 760 nm (Figure S1b, Supporting Information), respectively, cor-

responding to the intrinsic characteristics of $CH_3NH_3PbBr_3$ and $CH_3NH_3PbI_3$. At the heterojunction interface, both 535 and 760 nm peaks were observed (Figure S1c, Supporting Information). The sliced images across the heterojunction nanowire confirmed a uniform emission intensity distribution (Figure S2, Supporting Information). However, the anionic diffusion that commonly exists in a soft crystal lattice of hybrid halide perovskites[29] affected the emission stability of the printed heterojunction, as shown in the 1 week stability test (Figure S3, Supporting Information). We remark that the printed $CH_3NH_3PbBr_3$–$CH_3NH_3PbI_3$ nanowire exhibited a polycrystalline nature, as confirmed by selected-area electron diffraction (SAED) analysis in Figure 1e,f. The resulting material characteristics confirmed the practicality of our 3D printing method for perovskite heterostructures. In addition, we showed a remarkable process simplicity in integration: the heterojunction nanowire was directly printed on a Si substrate and a copper grid within 10 s, without any additional transfer process (Figure S4, Supporting Information).

Our 3D printing method offers a versatility to fabricate various combinations of heterojunctions. **Figure 2**a–c shows three exemplary combinations of $CH_3NH_3PbI_3$–$CH_3NH_3PbCl_3$ (Figure 2a), $CH_3NH_3PbBr_3$–$CH_3NH_3PbI_3$ (Figure 2b), and $CH_3NH_3PbBr_3$–$CH_3NH_3PbCl_3$ (Figure 2c). The FE-SEM images of these
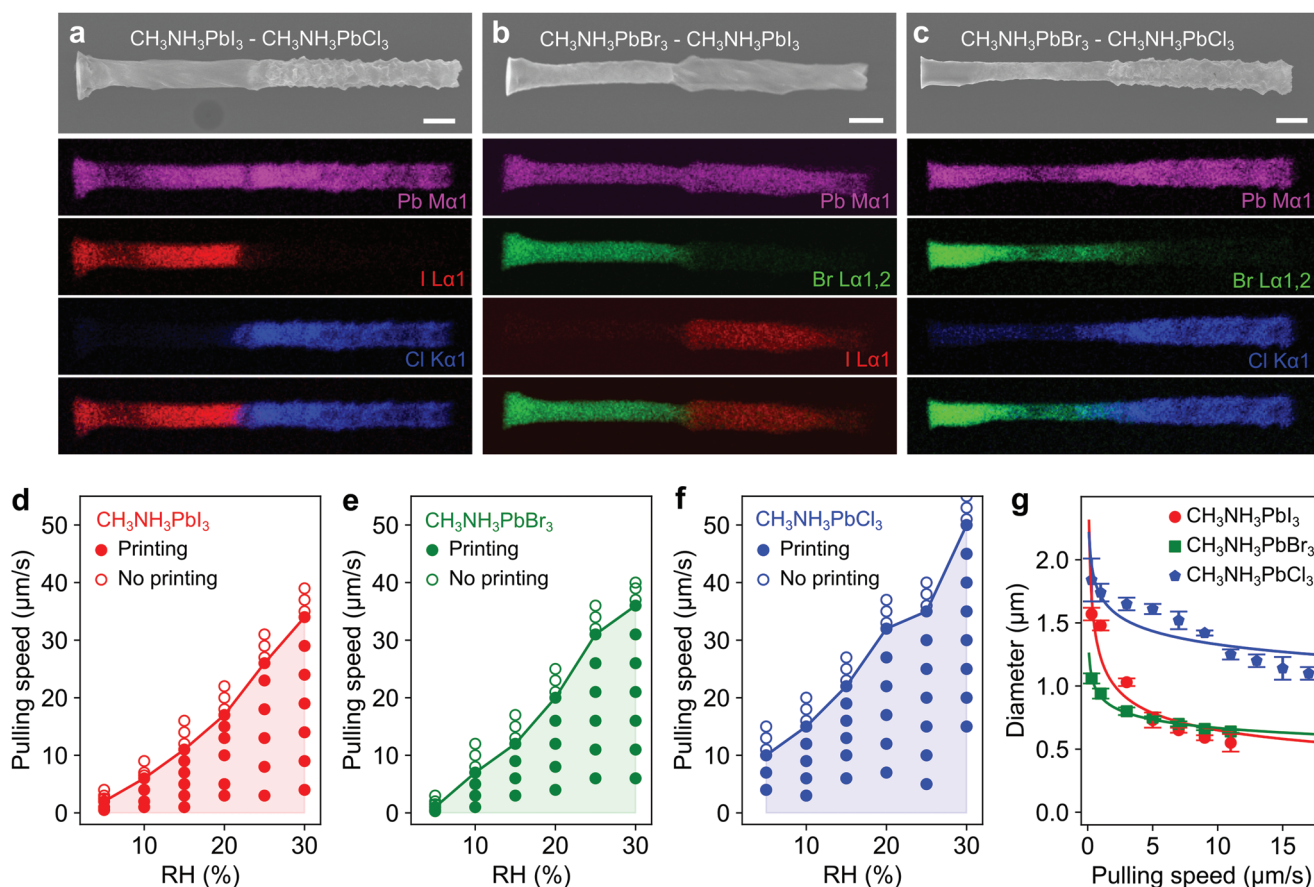

Figure 2. Elemental distributions and printing dynamics. a–c) FE-SEM and EDX images of printed perovskite heterojunctions with three different configurations, a) $CH_3NH_3PbI_3$–$CH_3NH_3PbCl_3$, b) $CH_3NH_3PbBr_3$–$CH_3NH_3PbI_3$, and c) $CH_3NH_3PbBr_3$–$CH_3NH_3PbCl_3$ (scale bar: 1 μm). d–f) Phase diagrams displaying the dependences of printability on the interplay between pulling speed of a nanopipette and humidity (RH%) for three different compositions, d) $CH_3NH_3PbI_3$, e) $CH_3NH_3PbBr_3$, and f) $CH_3NH_3PbCl_3$. Solid circles denote the success of printing, whereas open circles denote failure. Threshold pulling speeds are plotted in solid lines for each composition. g) Dependence of printed diameter on pulling speed.
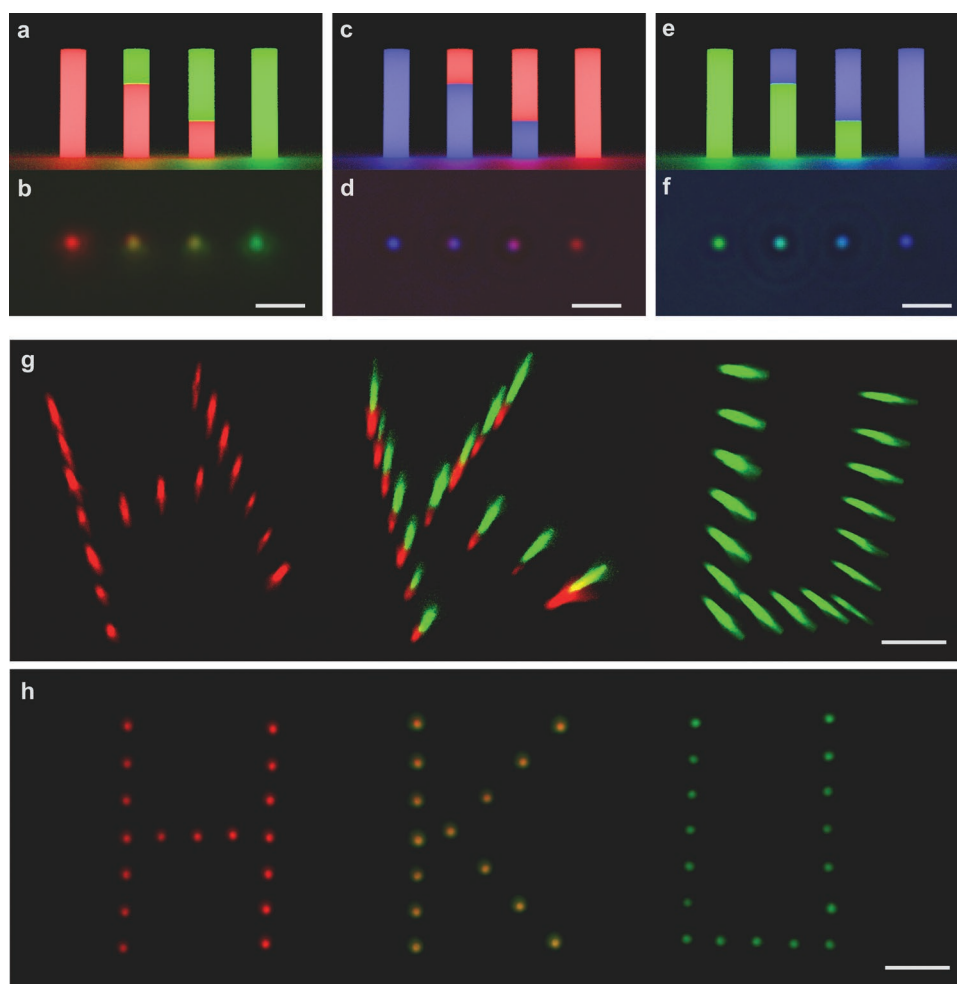
**ADVANCED
SCIENCE NEWS**

www.advancedsciencenews.com

**ADVANCED
FUNCTIONAL
MATERIALS**

www.afm-journal.de

Figure 3. Colored 3D nanopixels. a–f) Color mixing by adjusting length ratio. a) Scheme illustrating the color tuning from red to green by adjusting the length ratio of $CH_3NH_3PbI_3$ to $CH_3NH_3PbBr_3$ segments in a printed freestanding heterojunction from 1:0, 2:1, 1:2, to 0:1, and b) corresponding wide-field PL image (scale bar: 5 µm). c) Color tuning from blue to red by adjusting the length ratio of $CH_3NH_3PbCl_3$ to $CH_3NH_3PbI_3$ segments from 1:0, 2:1, 1:2, to 0:1, and d) corresponding wide-field PL image (scale bar: 5 µm). e) Color tuning from green to blue by adjusting the length ratio of $CH_3NH_3PbBr_3$ to $CH_3NH_3PbCl_3$ segments from 1:0, 2:1, 1:2, to 0:1, and f) corresponding wide-field PL image (scale bar: 5 µm). g,h) 3D printed multicolor pixel pattern. g) 3D confocal image of "HKU" nanopixel matrix. "H" consists of $CH_3NH_3PbI_3$ pixels, "K" consists of $CH_3NH_3PbI_3$–$CH_3NH_3PbBr_3$ heterojunction pixels, and "U" consists of $CH_3NH_3PbBr_3$ pixels (scale bar: 10 µm). h) Corresponding wide-field PL image (scale bar: 10 µm).

structures showed that their junctions are well connected. In addition, their elemental distributions were analyzed by energy-dispersive X-ray spectroscopy (EDS). Consistently, the halide compositions are clearly separated into two segments, whereas the lead is uniformly distributed along the printed nanowire.

A core engineering for continuous printing is to maintain a balance between the pipette moving speed and perovskite crystal growth. If the pipette moving is too fast, the printing is terminated. The maximum speed allowing continuous printing, defined as a threshold speed v_t, depends on the crystallization dynamics of perovskites. First, the dependence of threshold speed on relative humidity (RH) was investigated. Figure 2d shows the printing behavior of $CH_3NH_3PbI_3$ as a function of the interplay between the pipette pulling speed and RH ranging from 10% to 30%. Solid circles denote the success of printing, whereas open circles denote failure, and v_t is plotted in a solid line. A clear upward trend in v_t with RH is observed. This is in good agreement with previous studies revealing that mois-

ture accelerates the perovskite crystallization due to the hygroscopic property of methylammonium precursor.[43] The similar RH – v_t dependency was also found in the other compositions of $CH_3NH_3PbBr_3$ (Figure 2e) and $CH_3NH_3PbCl_3$ (Figure 2f). The quantitative difference among them is attributed to the supersaturation-driven crystallization rate depending on the compositions. Owing to the mechanical flexibility of the meniscus, the adjustment of the pulling speed allows the precise control of the printed diameter. Figure 2g shows the dependences of the printed diameter on the pulling speed for $CH_3NH_3PbI_3$ (red), $CH_3NH_3PbBr_3$ (green), and $CH_3NH_3PbCl_3$ (blue), respectively, at a constant RH of 10%. In all cases, the diameter decreases as the pulling speed increases. This quantitative investigation yields well-defined, reproducible perovskite heterojunctions with controlled dimensions (Figures S5 and S6, Supporting Information).

The 3D printed perovskite heterojunction can be a versatile nanopixel platform for photonic devices. The emission color of
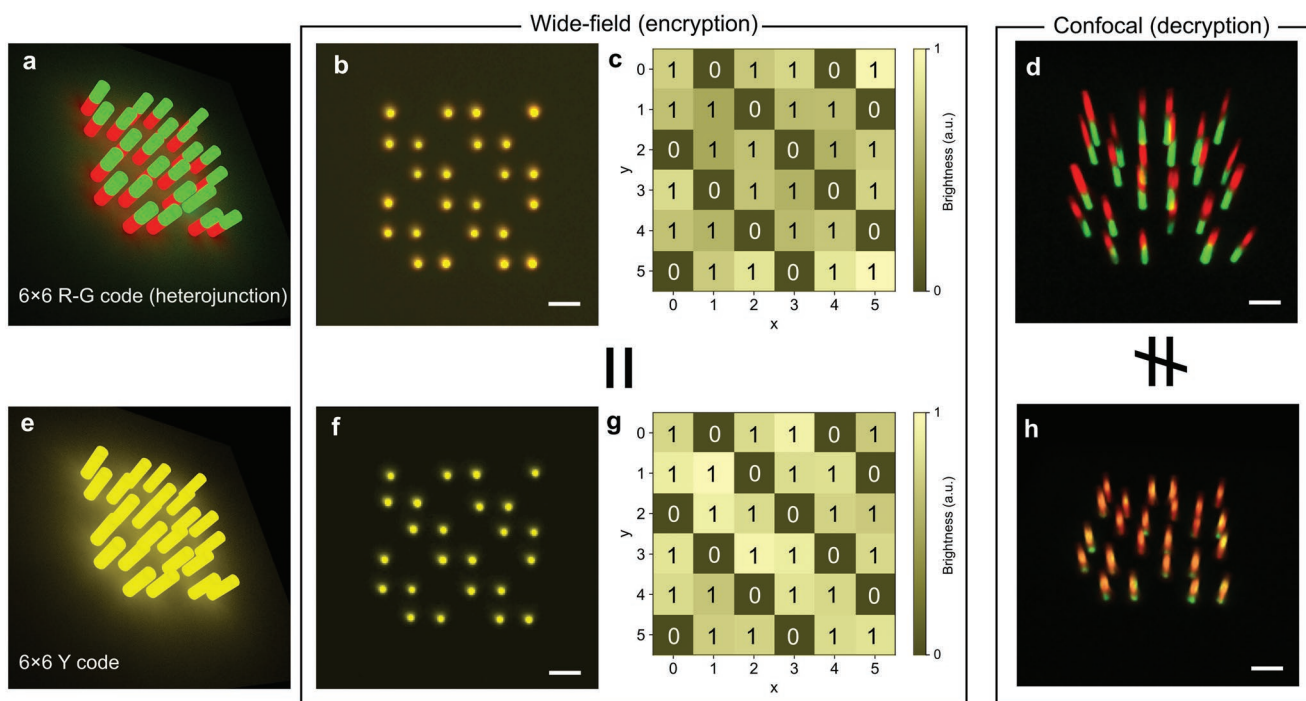
ADVANCED
SCIENCE NEWS
www.advancedsciencenews.com

ADVANCED
FUNCTIONAL
MATERIALS
www.afm-journal.de

Figure 4. Anticounterfeiting application. a–d) 6 × 6 matrix code comprising $CH_3NH_3PbI_3$–$CH_3NH_3PbBr_3$ red (R) – green (G) heterojunction pixels. a) Schematic design, b) wide-field PL image of the matrix code with yellow luminescence, and c) the corresponding binary information. d) Decrypted R-G code by 3D confocal imaging. e–h) 6 × 6 matrix code comprising $CH_3NH_3PbBr_{1.5}I_{1.5}$ yellow (Y) pixels. e) Schematic design, f) wide-field PL image of the matrix code with yellow luminescence, and g) the corresponding binary information. h) Decrypted Y code by 3D confocal imaging (scale bar: 5 μm).

a heterojunction nanowire can be readily tuned by varying the length ratio of the segments. Furthermore, its vertical configuration allows color tuning without the sacrifice of spatial resolution. **Figure 3**a illustrates vertical $CH_3NH_3PbI_3$–$CH_3NH_3PbBr_3$ nanopixels with different length ratios from 1:0, 2:1, 1:2, to 0:1. The height and diameter of these pixels are 2.5 μm and 600 nm, respectively. The top-view PL image of these nanopixels in Figure 3b clearly shows a gradual emission color change from red to green (from left to right) as the $CH_3NH_3PbBr_3$ segment length increases, under wide-field optical imaging configuration. Owing to the constant pixel height and diameter, no noticeable variation in the lateral emission size was observed. These features were also found from different combinations: the gradual color shift from blue to red by varying the length ratio of $CH_3NH_3PbCl_3$–$CH_3NH_3PbI_3$ (Figure 3c,d) and the green to blue varying the $CH_3NH_3PbBr_3$–$CH_3NH_3PbCl_3$ length ratio (Figure 3e,f).

Figure 3g,h shows an example of nanowire heterostructure-based color displays. A multi-color "HKU"-shaped nanopixel pattern was directly fabricated on a quartz substrate. A "H"-shaped emission with red color consists of an array of freestanding $CH_3NH_3PbI_3$ nanowires and a "U"-shaped emission with green color consists of an array of $CH_3NH_3PbBr_3$ nanowires. To implement yellow emission color in wide-field PL imaging, a "K"-shaped pattern consisting of an array of $CH_3NH_3PbI_3$–$CH_3NH_3PbBr_3$ heterojunction nanowires was integrated. This capability provides an on-demand configuration of displays with programmed color and shape at the sub-micrometer resolution.

The 3D-printed perovskite nanowire heterojunction with composition-determined emission colors can serve as a building block for high-resolution anticounterfeiting labels. A key security scheme is based on the inaccessibility of the spatial elemental distribution of vertical heterojunction pixels under a conventional wide-field PL microscope, as demonstrated in **Figure 4**. For example, we fabricated two 6 × 6 matrix codes having the similar color but different elemental distributions. Figure 4a,e depicts the designs of two 6 × 6 binary matrix codes comprising arrays of perovskite nanowires with the same height configuration: one consists of $CH_3NH_3PbI_3$–$CH_3NH_3PbBr_3$ heterojunction pixels (Figure 4a) and the other consists of $CH_3NH_3PbBr_{1.5}I_{1.5}$ pixels (Figure 4e). The wide-field PL images of these two codes showed the same binary pattern with similar color (yellow) (Figure 4b,f) . That is, their emission-intensity-based Quick Response (QR) digital codes quantitatively exhibit the same binary information, as shown in Figure 4c,g. Their elemental distributions can be decrypted only via high-resolution 3D imaging. As shown in Figure 4d,h, their confocal PL images and spectra are different. The $CH_3NH_3PbI_3$–$CH_3NH_3PbBr_3$ heterojunction pixel consisted of two clearly separated emission segments centered at 535 nm (green) and 760 nm (red), respectively. The emission of the $CH_3NH_3PbBr_{1.5}I_{1.5}$ pixel consisted of peaks centered at 610 nm (middle of the pixel body), 535 nm (bottom), and 730 nm (top) (Figure S7, Supporting Information) due to photo segregation. The result proves that the designed perovskite nanowire heterostructure offers a facile route to advance a level of security for anticounterfeiting applications. The data-storage capacity and
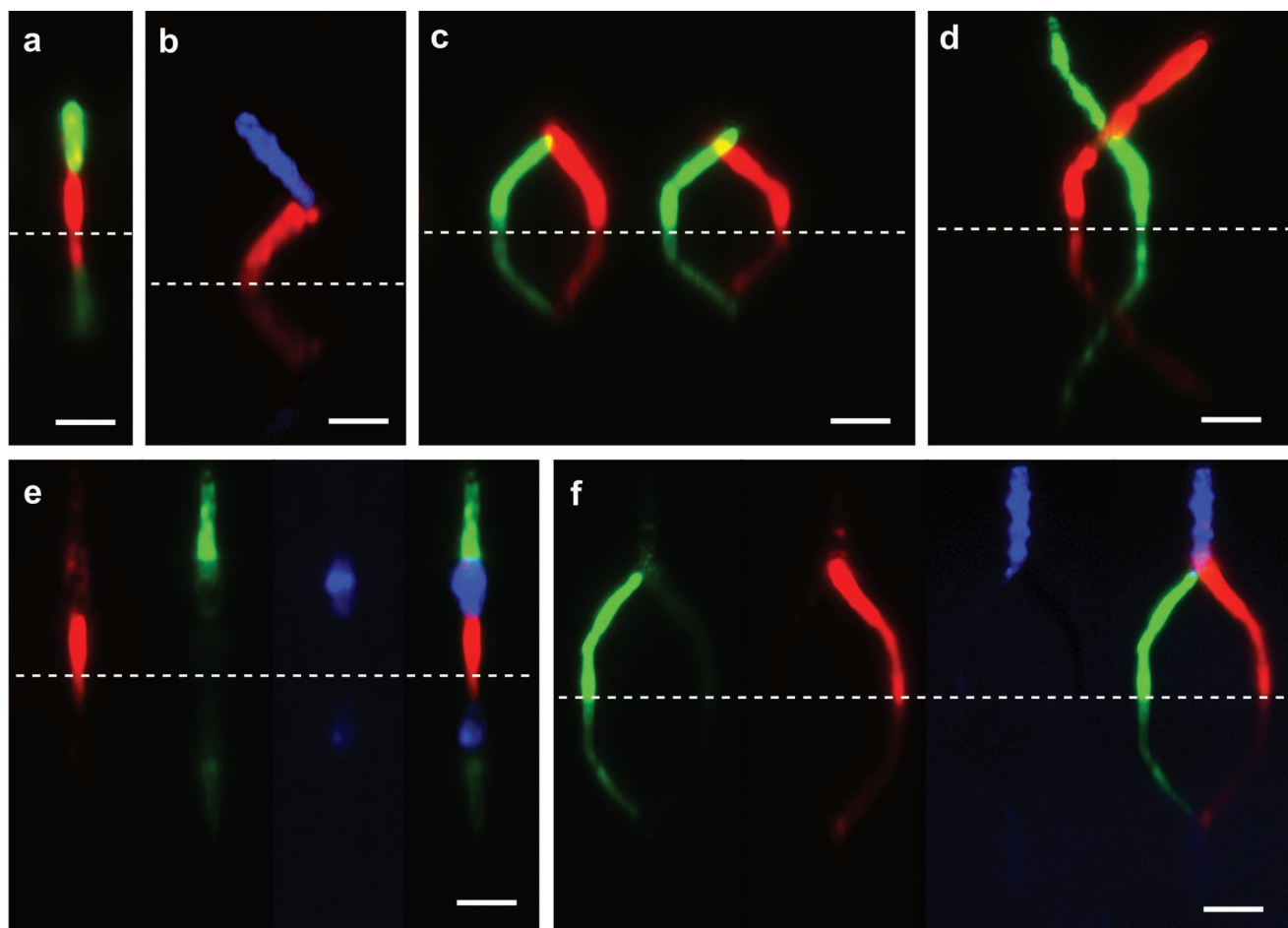
Figure 5. Freeform nanowire heterostructures. a) Straight two-color $CH_3NH_3PbI_3$–$CH_3NH_3PbBr_3$ wire, b) $CH_3NH_3PbI_3$–$CH_3NH_3PbCl_3$ zigzag, c) $CH_3NH_3PbI_3$–$CH_3NH_3PbBr_3$ arches, d) $CH_3NH_3PbI_3$–$CH_3NH_3PbBr_3$ intersection, e) three-colored $CH_3NH_3PbI_3$–$CH_3NH_3PbCl_3$–$CH_3NH_3PbBr_3$ barcode, and f) three-colored $CH_3NH_3PbBr_3$–$CH_3NH_3PbI_3$–$CH_3NH_3PbCl_3$ branch (scale bar: 5 µm). Dashed lines denote the substrate.

encryption level can further be enhanced by increasing compositional combinations.

The developed 3D printing method enables freeform, nanoscale integration of perovskite heterojunctions with programmed shape and composition. Successful examples have been demonstrated and their images have been captured by using a side-view wide-field fluorescence microscope (**Figure 5**). Figure 5a shows a straight two-color $CH_3NH_3PbI_3$–$CH_3NH_3PbBr_3$ nanowire heterojunction fabricated directly on the quartz substrate. Furthermore, a zig-zag shaped $CH_3NH_3PbI_3$–$CH_3NH_3PbCl_3$ junction was fabricated by tilting the printing direction (Figure 5b). The printed geometry can be further evolved, for example, $CH_3NH_3PbI_3$–$CH_3NH_3PbBr_3$ arches (Figure 5c) and a $CH_3NH_3PbI_3$–$CH_3NH_3PbBr_3$ intersection (Figure 5d). The fabrication of mutiple junctions were also demonstrated. Figure 5e shows a straight $CH_3NH_3PbI_3$–$CH_3NH_3PbCl_3$–$CH_3NH_3PbBr_3$ heterostructure with three-color emission, fabricated by using a triple meniscus guiding process. Furthermore, a freestanding triple nanojunction consisting of $CH_3NH_3PbI_3$, $CH_3NH_3PbBr_3$, and $CH_3NH_3PbCl_3$ segments was successfully fabricated (Figure 5f), showing the freeform printing capability. In addition, some exemplary structures consisting of ultralong perovskite nanowires printed in-plane or out-of-plane are demonstrated in Figure S8 (Supporting Information).

3. Conclusion

We have developed a minimalist, high-precision 3D printing method for creating arbitrary perovskite nanowire heterostructures. In contrast to the selected-area anion exchange or sequential growth approaches that take tens of hours, the developed meniscus-guided 3D printing offers simultaneous crystal growth and stacking with programmed shape, location, and composition, within seconds. A high-degree control over the elemental distribution in the printed heterojunction facilitates light-emissive nanopixels with tunable colors for displays and anticounterfeiting applications. Although in this work we restrict ourselves to $CH_3NH_3PbX_3$ (X = Cl,Br,I), the method can be generalized for various perovskites that are solution-processable if a thorough study of their crystallization dynamics confined in a femtoliter solution meniscus is performed. Also, further study on how to improve the crystalline quality in the printed structure would be necessary for practical use. These findings represent a milestone technological breakthrough for

fabricating semiconductor nanowire heterostructures, paving the new way for the fundamental science and engineering of optoelectronics.

4. Experimental Section

Materials: Methylammonium halide (CH$_3$NH$_3$I, CH$_3$NH$_3$Br, or CH$_3$NH$_3$Cl, purchased from GreatCell Solar) and lead(II) halide (PbI$_2$, PbBr$_2$, or PbCl$_2$ 99%, purchased from Sigma Aldrich) were mixed in a 1:1 molar ratio. The precursor ink was prepared by dissolving a 40 wt.% PbI$_2$–CH$_3$NH$_3$I, PbBr$_2$–CH$_3$NH$_3$Br, or PbCl$_2$–CH$_3$NH$_3$Cl mixture in the DMF (99.8%, purchased from Sigma Aldrich) and DMSO (99.7%, purchased from Sigma Aldrich) mixture (1:1 volume ratio). Each ink was stirred for 2 h at 60 °C. Double-barreled borosilicate nanopipettes (filament embedded; World Precision Instruments) were fabricated via a programmed heat-pulling process (P-97 Flaming/Brown Micropipette Puller, Sutter Instrument) and cut by the Focused Ion Beam equipped at HKU. These borosilicate nanopipettes and Si wafers were cleaned by 5 min ultrasonication in successive volumes of acetone, isopropyl alcohol, and deionized water.

3D Printing of Heterostructures: The printing setup consisted of a double-barreled nanopipette and a Si substrate, which were spatially controlled with submicron precision using a three-axis stepping motorized stage (XA05A, ZA05A, Kohzu Precision). The printing process was monitored in real time using a side-view optical microscope consisting of a 50× long-working-distance objective (Mitutoyo) and a camera equipped with a complementary metal oxide semiconductor sensor (DCC1545M, Thorlabs). The entire printing process was performed inside a custom-made environmental enclosure (filled with nitrogen gas) at a controlled relative humidity and temperature.

Sample Characterizations: The exteriors of the printed nanostructures were characterized by FE-SEM (Zeiss Leo 1530). The chemical compositions were quantitatively analyzed by EDS under a 20 kV electron beam. The optical PL images of the perovskite heterostructures were measured by fluorescence microscopy (Olympus CKX53, filter CKX3-RFA). The PL spectra of the perovskite heterostructures were measured using a micro-PL/Raman spectrometer under laser excitation at a wavelength of 364 nm. Confocal imaging was performed by confocal laser scanning microscopy (Nikon A1R), using a 40× oil-immersion objective lens. ImageJ software (National Institutes of Health, U.S.A.) was used to reconstitute the 3D images layer-by-layer along the z-axis. The side-view PL images were taken by using an inverted wide-field fluorescence microscope under 365 nm light excitation. To take side-view images, the samples were tilted 90°. For each sample, three images captured by a monochrome camera with red, green, and blue bandpass filters were post-colored in red, green, and blue, respectively, and merged. Prior to these characterizations, all the fabricated heterostructures were annealed at 100 °C for 30 min.

Supporting Information

Supporting Information is available from the Wiley Online Library or from the author.

Acknowledgements

Conflict of Interest

The authors declare no conflict of interest.

Data Availability Statement

Research data are not shared.

[1] A. Kojima, K. Teshima, Y. Shirai, T. Miyasaka, *J. Am. Chem. Soc.* **2009**, *131*, 6050.

[2] W. Nie, H. Tsai, R. Asadpour, J.-C. Blancon, A. J. Neukirch, G. Gupta, J. J. Crochet, M. Chhowalla, S. Tretiak, M. A. Alam, H.-L. Wang, A. D. Mohite, *Science* **2015**, *347*, 522.

[3] M. Liu, M. B. Johnston, H. J. Snaith, *Nature* **2013**, *501*, 395.

[4] H. Wei, D. DeSantis, W. Wei, Y. Deng, D. Guo, T. J. Savenije, L. Cao, J. Huang, *Nat. Mater.* **2017**, *16*, 826.

[5] Q. Jiang, L. Zhang, H. Wang, X. Yang, J. Meng, H. Liu, Z. Yin, J. Wu, X. Zhang, J. You, *Nat. Energy* **2017**, *2*, 16177.

[6] G. Xing, N. Mathews, S. S. Lim, N. Yantara, X. Liu, D. Sabba, M. Grätzel, S. Mhaisalkar, T. C. Sum, *Nat. Mater.* **2014**, *13*, 476.

[7] S. D. Stranks, G. E. Eperon, G. Grancini, C. Menelaou, M. J. P. Alcocer, T. Leijtens, L. M. Herz, A. Petrozza, H. J. Snaith, *Science* **2013**, *342*, 341.

[8] B. Chen, S.-W. Baek, Y. Hou, E. Aydin, M. D. Bastiani, B. Scheffel, A. Proppe, Z. Huang, M. Wei, Y.-K. Wang, E.-H. Jung, T. G. Allen, E. V. Kerschaver, F. P. G. d. A. Arquer, M. I. Saidaminov, S. Hoogland, S. D. Wolf, E. H. Sargent, *Nat. Commun.* **2020**, *11*, 1257.

[9] D. Shi, V. Adinolfi, R. Comin, M. Yuan, E. Alarousu, A. Buin, Y. Chen, S. Hoogland, A. Rothenberger, K. Katsiev, Y. Losovyj, X. Zhang, P. A. Dowben, O. F. Mohammen, E. H. Sargent, O. M. Bakr, *Science* **2015**, *347*, 519.

[10] G. Xing, N. Mathews, S. S. Lim, N. Yantara, X. Liu, D. Sabba, M. Grätzel, S. Mhaisalkar, T. C. Sum, *Nat. Mater.* **2014**, *13*, 476.

[11] D. Liu, T. L. Kelly, *Nat. Photonics* **2014**, *8*, 133.

[12] N. Wang, L. Cheng, R. Ge, S. Zhang, Y. Miao, W. Zou, C. Yi, Y. Sun, Y. Cao, R. Yang, Y. Wei, Q. Guo, Y. Ke, M. Yu, Y. Jin, Y. Liu, Q. Ding, D. Di, L. Yang, G. Xing, H. Tian, C. Jin, F. Gao, R. H. Friend, J. Wang, W. Huang, *Nat. Photonics* **2016**, *10*, 699.

[13] J. You, L. Meng, T.-B. Song, T.-F. Guo, Y. Yang, W.-H. Chang, Z. Hong, H. Chen, H. Zhou, Q. Chen, Y. Liu, N. D. Marco, Y. Yang, *Nat. Nanotechnol.* **2016**, *11*, 75.

[14] S. D. Stranks, H. J. Snaith, *Nat. Nanotechnol.* **2015**, *10*, 391.

[15] M. A. Green, A. Ho-Baillie, H. J. Snaith, *Nat. Photonics* **2014**, *8*, 506.

[16] W. Zhang, G. E. Eperson, H. J. Snaith, *Nat. Energy* **2016**, *1*, 16048.

[17] J. Huang, Y. Yuan, Y. Shao, Y. Yan, *Nat. Rev. Mater.* **2017**, *2*, 17042.

[18] X.-K. Liu, W. Xu, S. Bai, Y. Jin, J. Wang, R. H. Friend, F. Gao, *Nat. Mater.* **2021**, *20*, 10.

[19] S. D. Stranks, H. J. Snaith, *Nat. Nanotechnol.* **2015**, *10*, 391.

[20] K. Lin, J. Xing, L. N. Quan, F. P. G. d. Arquer, X. Gong, J. Lu, L. Xie, W. Zhao, D. Zhang, C. Yan, W. Li, X. Liu, Y. Lu, J. Kirman, E. H. Sargent, Q. Xiong, Z. Wei, *Nature* **2018**, *562*, 245.

[21] L. Gu, S. Poddar, Y. Lin, Z. Long, D. Zhang, Q. Zhang, L. Shu, X. Qiu, M. Kam, A. Javey, Z. Fan, *Nature* **2020**, *581*, 278.

[22] L. Dou, M. Lai, C. S. Kley, Y. Yang, C. G. Bischak, D. Zhang, S. W. Eaton, N. S. Ginsberg, P. Yang, *PNAS* **2017**, *114*, 7216.

[23] C. Fan, X. Xu, K. Yang, F. Jiang, S. Wang, Q. Zhang, *Adv. Mater.* **2018**, *30*, 1804707.

[24] E. Shi, Y. Gao, B. P. Finkenauer, Akriti, A. H. Coffey, L. Dou, *Chem. Soc. Rev.* **2018**, *47*, 6046.

[25] Y. Fu, W. Zheng, X. Wang, M. P. Hautzinger, D. Pan, L. Dang, J. C. Wright, A. Pan, S. Jin, *J. Am. Chem. Soc.* **2018**, *140*, 15675.

[26] B. Zhao, S. Bai, V. Kim, R. Lamboll, R. Shivanna, F. Auras, J. M. Richter, L. Yang, L. Dai, M. Alsari, X.-J. She, L. Liang, J. Zhang, S. Lilliu, P. Gao, H. J. Snaith, J. Wang, N. C. Greenham, R. H. Friend, D. Di, *Nat. Photonics* **2018**, *12*, 783.

[27] D. Pan, Y. Fu, N. Spitha, Y. Zhao, C. R. Roy, D. J. Morrow, D. D. Kohler, J. C. Wright, S. Jin, *Nat. Nanotechnol.* **2021**, *16*,159.

[28] M. L. Aubrey, A. S. Valdes, M. R. Filip, B. A. Connor, K. P. Lindquist, J. B. Neaton, H. I. Karunadasa, *Nature* **2021**, *597*, 355.

[29] Akriti, E. S. , S. B. Shiring, J. Yang, C. L. Atencio-Martinez, B. Yuan, X. Hu, Y. Gao, B. P. Finkenauer, A. J. Pistone, Y. Yu, P. Liao, B. M. Savoie, L. Dou, *Nat. Nanotechnol.* **2021**, *16*, 584.

[30] D. K. Schroder, *J. Appl. Phys.* **2003**, *94*, 1.

[31] R. Pillarisetty, *Nature* **2011**, *479*, 324.

[32] R. Doering, Y. Nishi, *Handbook of Semiconductor Manufacturing Technology*, CRC, Boca Raton **2008**.

[33] K. Able, K. Nordlund, J. Nord, A. Kuronen, *Phys. Rev. B* **2002**, *66*, 035205.

[34] P. D. Ye, G. D. Wilk, B. Yang, J. Kwo, S. N. G. Chu, S. Nakahara, H.-J. L. Gossmann, J. P. Mannaerts, M. Hong, K. K. Ng, J. Bude, *Appl. Phys. Lett.* **2003**, *83*, 180.

[35] P. R. Chidambaram, C. Bowen, S. Chakravarthi, C. Machala, R. Wise, *IEEE Trans. Electron Devices* **2006**, *53*, 944.

[36] E. Shi, B. Yuan, S. B. Shiring, Y. Gao, Akriti, Y. G. , C. Su, M. Lai, P. Yang, J. Kong, B. M. Savoie, Y. Yu, L. Dou, *Nature* **2020**, *580*, 614.

[37] Y. Wang, Z. Chen, F. Deschler, X. Sun, T.-M. Lu, E. A. Wertz, J.-M. Hu, J. Shi, *ACS Nano* **2017**, *11*, 3355.

[38] P. Guo, D. Liu, X. Shen, Q. Lv, Y. Wu, Q. Yang, P. Li, Y. Hao, J. C. Ho, K. M. Yu, *Nano Energy* **2022**, *92*, 106778.

[39] Q. Kong, A. Obliger, M. Lai, M. Gao, D. T. Limmer, P. Yang, *Nano Lett.* **2020**, *20*, 8151.

[40] M. Chen, J. Yang, Z. Wang, Z. Xu, H. Lee, H. Lee, Z. Zhou, S.-P. Feng, S. Lee, J. Pyo, S. K. Seol, D.-K. Ki, J. T. Kim, *Adv. Mater.* **2019**, *31*, 1904073.

[41] M. A. Skylar-Scott, J. Mueller, C. W. Visser, J. A. Lewis, *Nature* **2019**, *575*, 330.

[42] J. Hu, M.-F. Yu, *Science* **2010**, *329*, 313.

[43] G. E. Eperon, S. N. Habisreutinger, T. Leijtens, B. J. Bruijnaers, J. J. van Franeker, D. W. deQuilettes, S. Pathak, R. J. Sutton, G. Grancini, D. S. Ginger, R. A. J. Janssen, A. Petrozza, H. J. Snaith, *ACS Nano* **2015**, *9*, 9380.